

Real-Time 3D Simulation of Heat-Induced Air Turbulence

Wanqi Yuan
Clemson University
wanqiy@clemson.edu

Suren Jayasuriya
Arizona State University
sjayasur@asu.edu

Ethan Chung
University of Hawai'i at Mānoa
echung32@hawaii.edu

Huaijin Chen
University of Hawai'i at Mānoa
huaijin@hawaii.edu

Nianyi Li
Clemson University
nianyi1@clemson.edu

Man Luo
University of Hawai'i at Mānoa
mluo3@hawaii.edu

Jinwei Ye
George Mason University
jinweiye@gmu.edu

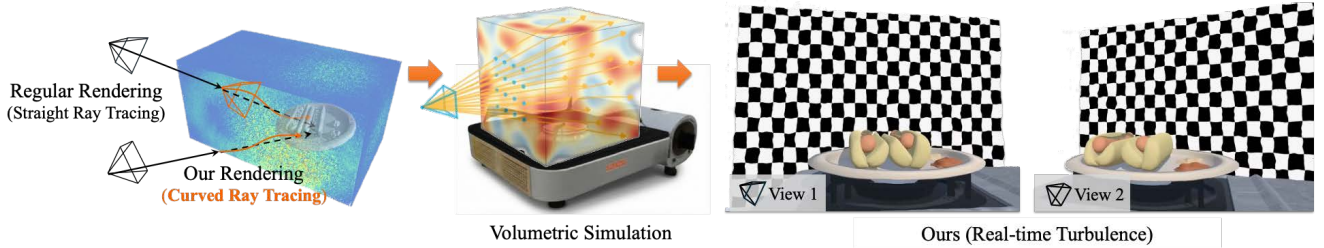


Figure 1. Overview of the proposed real-time heat-induced 3D fluid model and curved ray tracing approach. Rays traveling inside the fluid volume follow curved paths due to refractive index gradients, while rays outside the volume are rendered using standard straight ray tracing.

Abstract

Heat-induced air turbulence produces complex, depth-dependent image distortions that are challenging to reproduce interactively because thermally driven flow must be coupled with refractive light transport. Existing real-time methods often rely on single-view 2D screen-space warps that break multi-view coherence and do not model a 3D refractive volume. We present a real-time, fully 3D Lagrangian framework that models the full pipeline from thermal transport to density variation to optical refraction. Our system augments compressible Smoothed Particle Hydrodynamics (SPH) with temperature transport, buoyancy, and pressure-driven motion to capture rising plumes and turbulent mixing. We render the resulting continuous refractive-index field via curved ray tracing to model light bending in 3D. To reconcile physical fidelity with interactive performance, we introduce spatially adaptive step-size integration for curved-ray tracing, refining steps near strong refractive-index gradients while relaxing them in smooth regions to preserve temporal stability and high-frequency

distortion detail without uniform oversampling. The system runs at interactive rates (about 40fps in our prototype) and matches depth-dependent, multi-view-consistent distortions observed in real video captures more closely than image-based baselines.

1. Introduction

Heat-induced air turbulence underlies familiar optical phenomena such as heat haze above sun-baked roads and desert mirages. In computer graphics, synthesizing this effect is valuable for cinematic visual effects [42] and for generating controlled datasets for computer vision and imaging research [8, 31, 47, 57]. A central practical difficulty is that the visible distortion emerges from a coupled process: heat transport drives buoyant flow and density variation, which in turn induces a spatially varying refractive index that bends light. Capturing this chain in a way that is both *physically plausible* and *interactive* remains challenging—especially in multi-view settings, where inconsis-

tencies across viewpoints immediately degrade realism and depth perception.

Most existing approaches leave a key gap: they do not provide a shared, time-varying 3D refractive volume that multiple cameras can observe consistently. High-fidelity offline methods based on Eulerian solvers, including Lattice Boltzmann variants [21, 51, 59], can model thermally driven airflow and refraction with high accuracy, but their dense grid computations are typically too expensive for interactive use and large volumes. Conversely, many real-time methods are designed primarily as *image-space distortion generators* [7, 8, 47] by applying single-view screen-space warps (often procedural or simplified) to mimic turbulence. While effective for fast, view-dependent effects, these methods do not simulate a 3D medium and therefore cannot guarantee cross-view coherence or depth-dependent behavior when the same scene is observed from different viewpoints. This lack of coherence breaks immersion in inherently multi-view applications, such as VR/AR [5, 26], advanced flight simulation [38], and multi-camera scientific visualization [17, 46].

This paper targets a practical middle ground between these extremes. Our goal is not to replicate every fine-scale aspect of fully resolved fluid turbulence, but to produce *physically grounded and controllable* heat-haze behavior that arises from an explicit heat \rightarrow flow \rightarrow density \rightarrow refraction pipeline, and remains efficient enough for interactive simulation and rendering. To this end, we present a unified real-time framework that couples a compressible Lagrangian SPH-based thermofluid model with volumetric refractive rendering. Temperature evolves through heat exchange; buoyancy and pressure forces drive rising plumes and turbulent mixing; particle density is then mapped to a refractive-index field. Crucially, all cameras render through the same dynamic 3D refractive volume using curved ray integration, so multi-view coherence is enforced by construction rather than approximated in screen space. To further reconcile fidelity with real-time performance, we introduce a *spatially adaptive step-size strategy for curved-ray integration* that refines steps near strong refractive-index gradients (where high-frequency distortions originate) and takes larger steps in smooth regions, improving efficiency while maintaining temporal stability and distortion detail.

Additionally, we benchmark against *real-world captures* exhibiting heat-turbulence effects and compare to representative image-based turbulence simulators, focusing specifically on depth-varying distortions and multi-view 3D consistency. We will release our code, analysis scripts, and the real capture data to support reproducibility and future comparisons. Our major contributions are:

- We integrate heat-driven thermofluid simulation and volumetric refractive rendering into a single system that produces a shared 3D refractive volume observed consistently

from multiple viewpoints.

- We augment compressible SPH with temperature transport and buoyancy/pressure-driven motion to generate physically plausible plume dynamics and density variations suitable for real-time refractive rendering.
- We accelerate curved-ray integration by adapting step size to refractive-index variation, concentrating computation where distortions are visually significant and avoiding uniform oversampling elsewhere.
- We evaluate against real-world video captures and image-based baselines, highlighting the benefits of a true 3D volumetric model for cross-view consistency and depth-varying distortion.

2. Related Work

Richard Feynman famously stated that “Turbulence is the most important unsolved problem of classical physics” [13], and turbulent flow has been studied for centuries [12, 23, 24, 52]. Rather than survey this broad literature, we focus on work most relevant to our goal of real-time, multi-view-consistent heat-induced turbulence simulation and rendering.

SPH-Based Turbulence and Thermal Fluid Simulation.

Smoothed Particle Hydrodynamics (SPH) was introduced in astrophysics [15, 29] and later adopted in graphics for interactive fluid simulation [28, 30, 36, 45, 55]. Beyond early visually plausible effects, subsequent work explored more physically faithful turbulence modeling, often at higher computational cost [1, 9, 32, 34, 54]. Monaghan [9, 32] developed compressible α -turbulence models; Violeau [54] analyzed multiple SPH turbulence schemes; and Adami [1] studied detailed three-dimensional turbulence. For heat transfer, SPH has been applied to conduction and convection in particulate and complex flows [10, 22, 58]. More recent graphics work improves realism and robustness via vorticity-based detail enhancement [27], micropolar models for effects such as foam [3], and improved stability/convergence for both compressible and incompressible formulations [20]. While these methods advance SPH fidelity, they do not explicitly target the coupled dynamics characteristic of heat-induced air turbulence. We address this gap by extending [20] toward temperature-driven air turbulence suitable for real-time refractive rendering.

Real-Time Atmospheric Turbulence Simulation.

Real-time heat-haze simulation typically follows two directions: physics-based grid solvers and lightweight image-space distortions. Eulerian methods, notably GPU-accelerated Lattice Boltzmann schemes coupled with heat transfer, can reproduce mirages and heat shimmer but require large memory footprints for high fidelity [59]. In contrast, image-

based simulators model optical turbulence through phase screens [49], spatially varying point spread functions [6, 19], or phase-to-space transforms [8, 31]. These real-time approaches do not simulate a shared 3D refractive medium and therefore cannot guaranty multi-view coherence. Game engines often adopt procedural noise-based distortions [25, 39, 41], which are fast but lack correspondence to underlying flow or refractive-index dynamics. [48] introduced depth-dependent effects for image-based simulators using monocular depth estimation, but still without volumetric flow simulation. Our method aims for a practical middle ground: a simplified real-time volumetric thermofluid model that enables depth-dependent distortions and multi-view consistency.

Curved Ray Tracing in Inhomogeneous Media. Modeling light propagation through media with a spatially varying refractive index demands curved ray tracing algorithms that extend beyond straight-line assumptions. [4] first introduced layered Snell’s law tracing for mirages. [50] then employed Fermat’s principle to implement accurate curved-ray tracing in offline renderers, and [18] solved the physically-based differential equation governing light trajectories. Beyond atmospheric effects, adaptive numerical integration has been explored in gradient-index optics. For instance, [56] proposed an adaptive ray tracing algorithm for freeform media utilizing index directional derivatives to minimize error. However, these optical engineering methods typically prioritize extreme numerical precision for static media and rely on computationally heavy high-order solvers. While recent graphics research [2, 14, 40] provides rigorous transport solutions, they remain offline and unsuitable for interactive use. In contrast, our system introduces a lightweight adaptive stepping scheme driven by local ray curvature. This approach allows us to resolve the high-frequency density gradients of dynamic SPH turbulence without the overhead of optical design solvers, enabling efficient real-time rendering.

3. A Unified Model for Real-Time Heat-Induced Air Turbulence

As illustrated in Fig. 2, our model calculates heat transfer between particles and sources, translating temperature changes into buoyancy and convective forces. These forces drive motion within a state-of-the-art Smoothed Particle Hydrodynamics (SPH) framework, producing dynamic density variations. Finally, a curved ray-tracing renderer visualizes these density changes as multi-view consistent optical distortions.

3.1. Thermally-Driven Dynamics with SPH

We model air as a collection of particles within an SPH framework, a mesh-free, Lagrangian method ideal for dynamic fluids. Each particle i carries physical properties including mass m_i , position \mathbf{x}_i , velocity \mathbf{v}_i , density ρ_i , and temperature T_i :

$$i = \{m_i, \mathbf{x}_i, \mathbf{v}_i, \rho_i, T_i\} \quad (1)$$

The fluid state at any point is interpolated from neighboring particles using a smoothing kernel W , for which we employ Desbrun’s spiky kernel [35]. Unlike prior work targeting high-fidelity offline simulation, our goal is to capture the essential dynamics of heat-induced turbulence at interactive rates. The process begins by updating each particle’s temperature based on its interaction with heat sources and other particles. This new temperature field then generates forces that drive the fluid motion, as follows:

3.1.1. Heat Transport Model

There are two main interactions in our heat transport system:

1) Source-Particle Exchange: Our simulation injects thermal energy into the fluid through one or more user-defined heat sources, which are modeled as hexahedral regions in space. The total heat Q at position \mathbf{x} with temperature T during a single time step is the sum of the individual contributions from all n sources present in the scene:

$$Q(\mathbf{x}, T) = \sum_s q_s(\mathbf{x}, T), \quad (2)$$

where q_s is the heat flux from an individual source s . The calculation of q_s is designed to be localized and is fundamentally driven by the temperature difference between the source T_s and the particle T . To ensure a smooth falloff, the model defines an “influence zone” of radius R_s around each source, and the amount of heat transferred decays linearly with the distance from the source’s boundary. The heat flux from source s therefore given by the piecewise function:

$$q_s(\mathbf{x}, T) = \begin{cases} (T_s - T) \lambda_s r \Delta t, & \text{if } \mathbf{x} \text{ lies} \\ & \text{inside the} \\ & \text{source,} \\ (T_s - T) \lambda_s r \Delta t \left(1 - \frac{d_s}{R_s}\right), & \text{if } d_s < R_s, \\ 0, & \text{otherwise.} \end{cases} \quad (3)$$

where d_s represents the shortest distance from the particle to the surface of source s , λ_s is a user-defined influence coefficient controlling the source’s strength, r the heat-transfer rate between sources and particles, and Δt the simulation time-step.

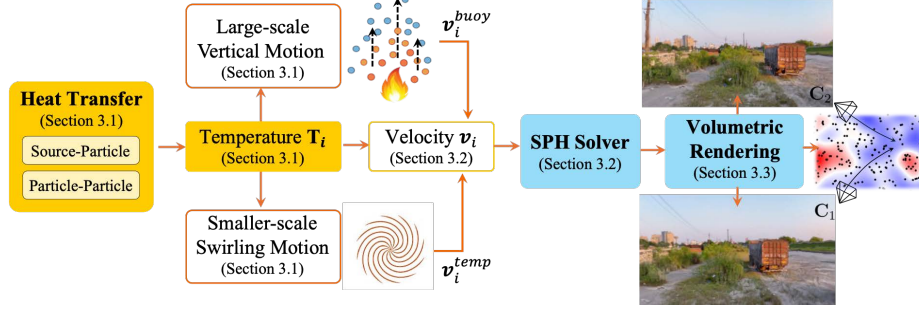


Figure 2. Overview of the simulation and rendering pipeline. The system models heat transfer through source-particle and particle-particle interactions, updating temperature, buoyancy, and velocity accordingly. These attributes drive updates to particle position, density, and pressure. The updated particle states are rendered via curved ray tracing through camera views C_1, C_2 .

2) Inter-Particle Conduction: To model the diffusion of heat throughout the fluid, we start from the continuous form of the Fourier heat-conduction equation [11], which governs transient heat flow:

$$\rho c \frac{\partial T}{\partial t} = \nabla \cdot (k \nabla T) + Q, \quad (4)$$

where ρ is the material density, c the specific heat capacity, T the temperature field, t time, k the thermal conductivity, and Q is the energy from external heat sources. The operator $\nabla \cdot (\cdot)$ denotes the divergence, while ∇T is the temperature gradient.

To adapt this for our SPH particle system, we must discretize it. However, directly discretizing the second-order derivatives in $\nabla \cdot (k \nabla T)$ can lead to numerical instability. We therefore adopt the more robust pairwise heat-transfer formulation from [37], which models conduction as a one-dimensional heat exchange along the line connecting each particle pair (i, j) . This approach enforces energy conservation and improves stability. The resulting SPH discretization for the rate of temperature change of particle i due to conduction is:

$$\frac{\partial T_i}{\partial t} = \frac{1}{\rho_i c_i} \sum_j \frac{m_j}{\rho_j} \cdot \frac{4k_i k_j}{k_i + k_j} \cdot \frac{\mathbf{r}_{ij} \cdot \nabla_i W_{ij}}{\|\mathbf{r}_{ij}\|^2} \cdot (T_j - T_i), \quad (5)$$

where the sum is over all neighboring particles j . Here, m_j and ρ_j are the mass and density of particles j , k_i and k_j are their thermal conductivities, $\mathbf{r}_{ij} = \mathbf{r}_i - \mathbf{r}_j$ is the vector between them, and $\nabla_i W_{ij}$ is the gradient of the smoothing kernel W (Desbrun’s spiky kernel).

For our specific case of simulating air, we introduce two simplifying assumptions to enhance real-time performance. We assume a constant specific heat capacity ($c_i = 1$) and a uniform thermal conductivity $k_i = k_j = k$ for all particles. This reduces the full equation to a more computationally efficient form:

$$\frac{\partial T_i}{\partial t} = \frac{1}{\rho_i} \sum_j \left[\frac{2km_j}{\rho_j} \cdot \frac{\mathbf{r}_{ij} \cdot \nabla_i W_{ij}}{\|\mathbf{r}_{ij}\|^2} \cdot (T_j - T_i) \right]. \quad (6)$$

While not strictly physical, this is a deliberate design choice that plausibly enhances turbulent detail at a negligible computational cost, which is essential for achieving real-time performance.

3.1.2. Thermal Force Generation.

Once the temperature field is updated through conduction and source interactions, the next step is to translate these *thermal changes* into *particle motion*. Our system accomplishes this with a simplified thermal force model designed to be both computationally efficient and visually plausible. This model captures the two primary effects of heated air:

1) Large-scale vertical motion. The dominant effect is *Buoyancy force* \mathbf{F}^{buoy} , which we model based on Archimedes’ principle:

$$\mathbf{F}^{\text{buoy}} = (\rho_{\text{env}} - \rho_s) g V, \quad (7)$$

where $(\rho_{\text{env}} - \rho_s)$ is the density difference between the ambient and heated gases, g is the gravitational acceleration, and V is the volume. To make this efficient for our particle system, we use a linearized density–temperature relation ($\rho \approx -K T$). This allows us to express the buoyancy force directly in terms of temperature difference:

$$\mathbf{F}_i^{\text{buoy}} = K (T_i - T_{\text{env}}) g V. \quad (8)$$

This force is then used to compute the buoyancy-induced velocity change for each particle i over the time step Δt :

$$\Delta \mathbf{v}_i^{\text{buoy}} = \frac{\mathbf{F}_i^{\text{buoy}}}{\rho_i} \Delta t \quad (9)$$

2) Smaller-scale swirling motion. In addition to the large-scale motion from buoyancy, we introduce a *convective velocity term* to enhance smaller-scale turbulent details. This is a deliberate design choice for visual plausibility, where we assume particles tend to accelerate toward regions

of increasing temperature. This effect is modeled as a simple velocity increment:

$$\Delta \mathbf{v}_i^{\text{temp}} = \beta \frac{\nabla T_i}{\|\nabla T_i\|}, \quad (10)$$

where β is a user-defined multiplier that controls the strength of the effect. $\nabla T_i / \|\nabla T_i\|$ is the unit vector in the direction of steepest temperature increase. While not physically rigorous, this model provides an inexpensive way to add swirling motion that is crucial for the final visual appearance.

These two components are combined to produce a total thermal velocity update:

$$\Delta \mathbf{v}_i^{\text{thermal}} = \Delta \mathbf{v}_i^{\text{buoy}} + \Delta \mathbf{v}_i^{\text{temp}} \quad (11)$$

This total update is applied at the beginning of each simulation time step, serving as the primary driver for the fluid’s motion before the SPH solver resolves the pressure and density constraints.

3.2. SPH Solver and State Update

Next, we apply SPH solver to all particles, and update their state accordingly. Note that our thermal force model is designed to be modular and can be seamlessly integrated into *any efficient SPH framework* as an external force update. For our implementation, we chose the recent semi-implicit SPH solver by He et al. [20] to serve as the computational backbone.

At each simulation step, we perform three stages (see the full algorithm in the supplementary material): *1) Thermal prediction (external update)*. We first update temperature via heat exchange and apply the resulting buoyancy/thermal acceleration to obtain predicted velocities and an intermediate position \mathbf{x}_i^* . This stage injects the heat-driven dynamics that generate plumes and turbulence. *2) SPH constraint solve (backbone)*. Starting from \mathbf{x}_i^* , we run the SPH solver to enforce the fluid constraints (e.g., constant density) by iteratively correcting particle positions, resolving pressure effects through the solver’s optimization procedure. *3) State update*. Finally, we update the particle velocity from the net displacement over the time step, ensuring the state reflects both the thermal forcing (Stage 1) and the solver’s pressure corrections (Stage 2).

Figure 4 illustrates this process: a localized heat source drives initially stationary particles into a rising convective plume (blue→red velocity transition), dynamically reshaping the density field required for the subsequent refractive rendering.

3.3. Volumetric Rendering of Optical Distortions

Heat haze is visible because density variations in air induce a spatially varying refractive index, bending light rays and

producing depth-dependent distortions. Our renderer therefore converts the simulated density field into a refractive-index volume and traces *curved* rays through this inhomogeneous medium.

3.3.1. Refractive Index from Density:

We first rasterize the particle densities into a regular 3D grid (resolution \mathbf{R}) and evaluate a continuous density field $\rho(\mathbf{x})$ via SPH kernel splatting at voxel centers. We then map density to refractive index using the Gladstone–Dale relation [16]:

$$n(\mathbf{x}) = 1 + K_{\text{GD}} \cdot \rho(\mathbf{x}), \quad (12)$$

where K_{GD} is the Gladstone–Dale constant. Crucially, the ray curvature is driven by the refractive-index gradient, which is directly proportional to the density gradient:

$$\nabla n(\mathbf{x}) = K_{\text{GD}} \cdot \nabla \rho(\mathbf{x}). \quad (13)$$

In practice, we compute $\nabla \rho$ on the grid using finite differences and sample both $n(\mathbf{x})$ and $\nabla n(\mathbf{x})$ along the ray with trilinear interpolation.

3.3.2. Curved Ray Tracing Through the Refractive Volume

Let a camera ray follow a curve $\mathbf{C}(s) \in \mathbb{R}^3$ parameterized by arc length s , with unit tangent (ray direction) $\boldsymbol{\omega}(s) = \frac{d\mathbf{C}}{ds}$ and $\|\boldsymbol{\omega}(s)\| = 1$. In an inhomogeneous refractive medium, the ray path satisfies the standard vector ray equation (from Fermat/Eikonal optics):

$$\frac{d}{ds} \left(n(\mathbf{C}(s)) \boldsymbol{\omega}(s) \right) = \nabla n(\mathbf{C}(s)). \quad (14)$$

Expanding Eq. (14) yields an ODE for the change in direction that depends only on the component of ∇n *perpendicular* to the ray:

$$\frac{d\boldsymbol{\omega}}{ds} = \frac{1}{n(\mathbf{C}(s))} \left(\mathbf{I} - \boldsymbol{\omega} \boldsymbol{\omega}^\top \right) \nabla n(\mathbf{C}(s)). \quad (15)$$

We integrate Eq. (15) with a simple, stable explicit update. At step k (position \mathbf{C}_k , direction $\boldsymbol{\omega}_k$), let $n_k = n(\mathbf{C}_k)$ and $\mathbf{g}_k = \nabla n(\mathbf{C}_k)$. We update:

$$\begin{aligned} \boldsymbol{\omega}_{k+1} &= \text{normalize} \left(\boldsymbol{\omega}_k + \frac{\Delta s_k}{n_k} \left(\mathbf{I} - \boldsymbol{\omega}_k \boldsymbol{\omega}_k^\top \right) \mathbf{g}_k \right), \\ \mathbf{C}_{k+1} &= \mathbf{C}_k + \Delta s_k \boldsymbol{\omega}_{k+1}. \end{aligned} \quad (16)$$

Because clear air is effectively non-participating, we ignore absorption/scattering/emission and generate the image purely from ray bending: each pixel samples the scene radiance along the refracted ray via standard scene intersection (accelerated as described below).



Figure 3. Our simulation and rendering results. For a complete set of better visual effects, please see Figure 8, and the dynamic video results in Supplementary materials.

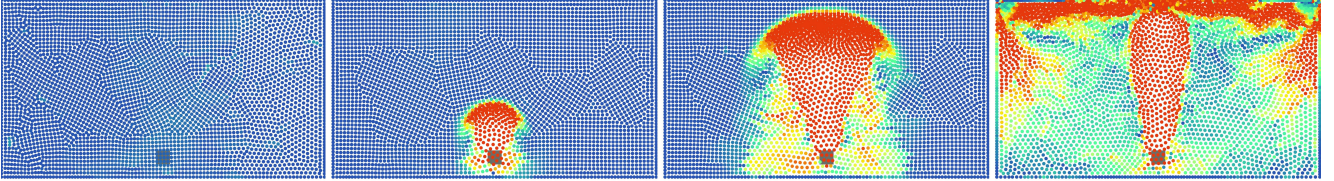


Figure 4. 2D dissection of our heat-driven particle system. The bottom square marks the heat source. Initially (left), the system is quiescent. Once activated, particles absorb heat, rise, and spread turbulence throughout the domain (left to right). Colors denote velocity magnitude, from slow (blue) to fast (red).

3.3.3. Adaptive Step Size for Efficient and Stable Ray Integration

A fixed step size wastes work in smooth regions and can miss high-frequency distortions near sharp refractive-index gradients (e.g., near plume boundaries). We therefore choose Δs_k adaptively using the local *angular change rate* of the ray direction. From Eq. (15), the local curvature magnitude is

$$\kappa_k = \left\| \frac{d\omega}{ds} \right\| = \frac{1}{n_k} \left\| \left(\mathbf{I} - \omega_k \omega_k^\top \right) \mathbf{g}_k \right\|. \quad (17)$$

We then bound the maximum turning angle per step by a user-specified tolerance θ_{\max} (in radians) and compute:

$$\begin{aligned} \Delta s_k &= \text{clamp} \left(\frac{\theta_{\max}}{\kappa_k + \varepsilon}, \Delta s_{\min}, \Delta s_{\max} \right) \\ &= \text{clamp} \left(\frac{n_k \theta_{\max}}{\left\| \left(\mathbf{I} - \omega_k \omega_k^\top \right) \mathbf{g}_k \right\| + \varepsilon}, \Delta s_{\min}, \Delta s_{\max} \right), \end{aligned} \quad (18)$$

where ε avoids division by zero and $\Delta s_{\min}, \Delta s_{\max}$ bound the step length for robustness. Intuitively, by Eq. (13) the refractive-index gradient scales with the density gradient, so regions with large $\|\nabla \rho\|$ induce higher ray curvature (Eq. (17)) and therefore require smaller steps in Eq. (18) to bound the per-step angular error, as shown in Fig. 5.

4. Experimental Results

We evaluate our system along three axes: (1) **real-time performance** and scalability, (2) **physical plausibility** of volumetric heat-haze distortions, and (3) our key capability:

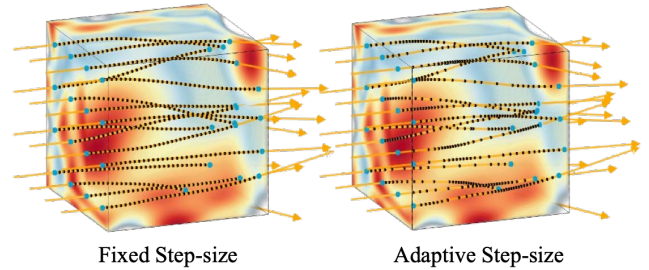


Figure 5. 3D illustration of curved ray tracing with adaptive step size. Red regions indicate higher density, while blue regions indicate lower density. We can tell that our adaptive step size implementation can effectively reduce the sampling points during ray-tracing.

multi-view consistent rendering from a single 3D turbulence volume. We compare to representative image-based turbulence simulators and validate against a controlled real capture.

4.1. Implementation and Settings

We implement SPH simulation in Unity compute shaders and curved ray marching in fragment shaders. All experiments run on an NVIDIA RTX 4090 (24 GB) with an Intel i9-13900K. Unless otherwise specified, we use $\Delta t=0.006s$ and $N \in [0.5, 1.5]$ M particles for interactive frame rates. Key parameters include thermal conductivity $k = 100$, buoyancy constant $K = 100$, convection multiplier $\beta = 50$, smoothing radius $H = 0.1$, and reference density $\rho_0 = 300 \text{ kg/m}^3$ (for air at room temperature). For completeness and stress-testing, we also support a fixed-step variant by set-

Table 1. Mean FPS on an NVIDIA RTX 4090 (24 GB) at 1920×1080. Each entry reports **Adaptive/Static** step-size curved-ray tracing (static $\Delta s=0.02$). Baseline (when not varied): $N=1.5\text{M}$, grid 10^3 , 1 camera.

Particles N (millions)					
Values	0.50	0.10	1.5	2.00	2.5
FPS \uparrow	75.5/50.6	49.3/35.1	35.1/25.5	25.7/20.5	18.9/17.5
Grid Resolution					
Values	10^3	15^3	20^3	25^3	30^3
FPS \uparrow	35.1/25.5	41.2/25.0	43.0/25.4	42.2/23.9	43.5/22.6
# Cameras					
Values	1	2	3	4	5
FPS \uparrow	35.1/25.5	27.0/20.3	23.4/16.4	21.2/13.8	20.2/12.5

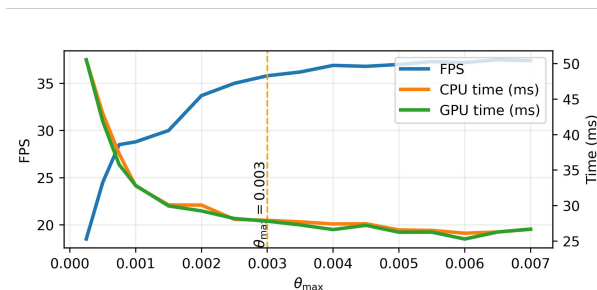


Figure 6. FPS, CPU time, and GPU time versus the error tolerance θ_{\max} .

ting $\Delta s_k \equiv \Delta s$. A full list is provided in a table in the supplemental material.

Acceleration via SDF shell. To avoid expensive ray-triangle tests for every refracted segment, we precompute a conservative SDF *shell* around scene geometry. During marching, we test the refracted ray against the shell and perform exact intersections only after entering it.

Scalability. Tab. 1 reports scalability with respect to particle count, grid resolution, and number of simultaneous camera views. Each entry shows **Adaptive/Static** step-size curved-ray tracing (static $\Delta s=0.02$), demonstrating that adaptive stepping substantially improves throughput while retaining the same volumetric model.

Adaptive tolerance sweep. Fig. 6 shows the accuracy-speed trade-off controlled by the maximum turning angle per step θ_{\max} (Eqn. 18). Increasing θ_{\max} increases the mean step size and improves FPS until diminishing returns; we set $\theta_{\max} = 0.003$ for all adaptive experiments.

4.2. Validation and Comparative Analysis

We compare against representative image-based turbulence simulators: DAAT-Sim [48], QuickTurb [47], TurbulenceSimP2S [31], and ATsyn [57]. Note that these methods operate in 2D (screen-space), and cannot enforce *geometrically consistent* distortions across viewpoints. Instead, our method renders from a persistent 3D refractive-index field. Since no prior work provides a real-time 3D *multi-view* heat-haze simulator with a shared refractive volume, these baselines represent the closest alternatives commonly used in practice.

Real-capture benchmark. We adopt a controlled laboratory setup similar to that of Tian et al. [53], as shown in Fig. 7. Three adjacent electric cooking griddles, each 52cm × 26cm, are heated to 400°F to generate a consistent and controllable volume of thermal turbulence. A reference checkerboard scene is observed through this volume, a setup which allows for the emulation of various outdoor turbulence strengths equivalent to a path-length of several kilometers. To analyze the distortion, video sequences of the scene are captured at 30 fps. We captured videos using two GoPro HERO11 Black Mini cameras at a 5.3K resolution with an aperture of $f/2.5$, operating in Linear mode to avoid lens edge distortion.

Depth-dependent distortion (volumetric property). A key advantage of our 3D simulation is its ability to correctly model how optical distortions accumulate over distance. This volumetric property, as discussed in [53], can be viewed as a depth-dependent distortion effect, which is absent in screen-space methods. Following the physical model in [53], the variance $\langle \alpha^2 \rangle$ of the angle-of-arrival fluctuations from a scene point at distance L from the camera, under a constant turbulence strength C_n^2 is:

$$\langle \alpha^2 \rangle = 2.914 D^{-1/3} C_n^2 \int_0^L \left(\frac{z}{L} \right)^{5/3} dz = \frac{3}{8} K_n^2 L, \quad (19)$$

where $K_n^2 = 2.914 D^{-1/3} C_n^2$ and D denotes the aperture diameter. We validate that our simulator adheres to this physical principle in two settings:

1) *Discrete Depths:* We place two checkerboards at different distances from the camera (Fig. 7). By tracking markers on each board, we measure the variance of their apparent motion. The results show two distinct clusters of variance, with the farther checkerboard exhibiting significantly higher variance, consistent with the theoretical model and real-world observations.

2) *Continuous Depth:* We place a single checkerboard slanted with respect to the camera plane. As shown in Fig. 7, the measured variance of markers on the board increases linearly with their distance from the camera, con-

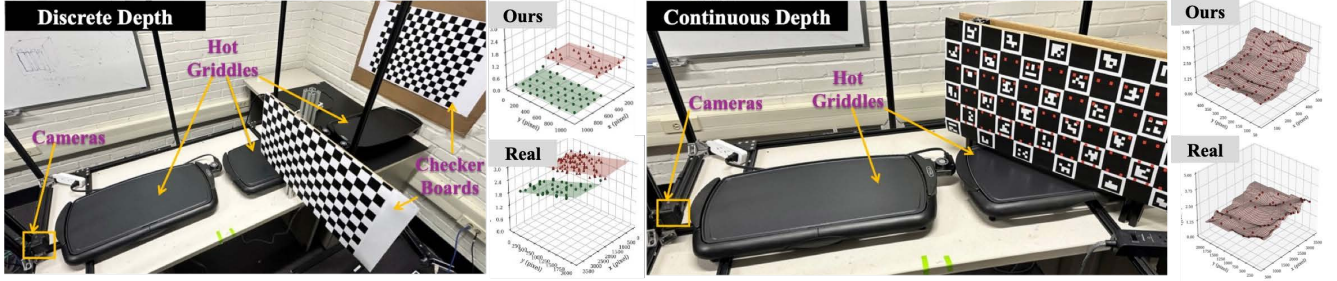


Figure 7. Under constant turbulence strength, the angle-of-arrival variance grows linearly with distance. We validate this trend in two configurations: (1) Discrete depths with two parallel checkerboards at different L (farther plane yields larger variance), and (2) Continuous depth using a slanted checkerboard, where variance increases approximately linearly along the depth gradient. Our simulated results matches the real-captured trend (More results in Figure Page).

firming that our simulation correctly integrates distortion along the view path.

Multi-view consistency. The central contribution of our work is the ability to render a single, coherent turbulence volume from multiple viewpoints simultaneously. Unlike 2D image-based simulators that apply an independent, random distortion to each frame, our simulator’s use of a persistent 3D density field and curved ray tracing naturally preserves multi-view coherence. Specifically, we place two cameras with a small baseline observing the same turbulence volume and track checkerboard markers in both views. We compare the cross-view displacement distributions using KL divergence as well as mean-squared error for these curves. Tab. 2 shows our simulator produces substantially lower divergence and MSE than image-based baselines and approaches real capture consistency.

Table 2. KL-divergence (KLD) and mean-squared error (MSE) between the cross-view displacement distributions of tracked points (lower is better), ours reports **Adaptive/Static** step-size results. **Real capture** provides the reference consistency measured from two synchronized cameras.

Metric	DAAT-Sim	QuickTurb	TurbSim P2S	ATsyn	Ours	Real
KLD-X ↓	0.0204	0.1935	0.0370	0.0353	0.0137/0.0210	0.0005
KLD-Y ↓	0.0205	0.1751	0.0216	0.0334	0.0176/0.0158	0.0005
MSE-X ↓	0.0276	0.0554	0.0189	0.0204	0.0055/0.0079	0.0006
MSE-Y ↓	0.0193	0.0582	0.0191	0.0155	0.0062/0.0059	0.0008

4.3. Ablation Study

To validate our thermal forcing design, we disable buoyancy and convection terms in isolation and quantify how the resulting flow dynamics change. We report two standard turbulence statistics: **turbulent kinetic energy (TKE)**, which measures the energy in velocity fluctuations, and **mean vorticity magnitude**, which captures rotational (swirling) content associated with turbulent eddies [44].

Metrics. Given particle velocities $\{\mathbf{v}_i\}_{i=1}^N$ with masses $\{m_i\}$, let $M = \sum_i m_i$ and the mass-weighted mean velocity $\bar{\mathbf{v}} = \frac{1}{M} \sum_{i=1}^N m_i \mathbf{v}_i$. We compute TKE per unit mass as the mean kinetic energy in the fluctuating component $\mathbf{v}_i - \bar{\mathbf{v}}$:

$$\text{TKE} = \frac{1}{2M} \sum_{i=1}^N m_i \|\mathbf{v}_i - \bar{\mathbf{v}}\|^2, \quad (20)$$

(which reduces to $\frac{1}{2N} \sum_i \|\mathbf{v}_i - \bar{\mathbf{v}}\|^2$ for equal-mass particles). TKE is widely used to summarize turbulence intensity and its evolution [44].

To measure rotational structure, we estimate each particle’s vorticity via the standard SPH curl operator [33]:

$$\boldsymbol{\omega}_i = \sum_j \frac{m_j}{\rho_j} (\mathbf{v}_j - \mathbf{v}_i) \times \nabla_i W_{ij}, \quad \|\boldsymbol{\omega}\| = \frac{1}{N} \sum_{i=1}^N \|\boldsymbol{\omega}_i\|. \quad (21)$$

Vorticity-based measures are commonly used to analyze or enhance turbulent details in graphics-oriented particle solvers [27, 43].

Tab. 3 shows that **buoyancy-only** produces weak motion with low TKE and vorticity, while **convection-only** increases local fluctuations but remains less energetic overall. The **full model** achieves the highest TKE and mean vorticity, confirming that buoyancy injects large-scale energy and convection promotes smaller-scale swirling, together producing richer and more plausible turbulence.

Table 3. Ablation study of our thermal force model. We compare the full model against versions with key components disabled, using quantitative turbulence metrics (Mean Vorticity and TKE) to validate our design choices.

Model Component	Mean Vorticity	TKE
Buoyancy Only	8.078	0.052
Convection Only	8.681	0.073
Full Model	8.919	0.086

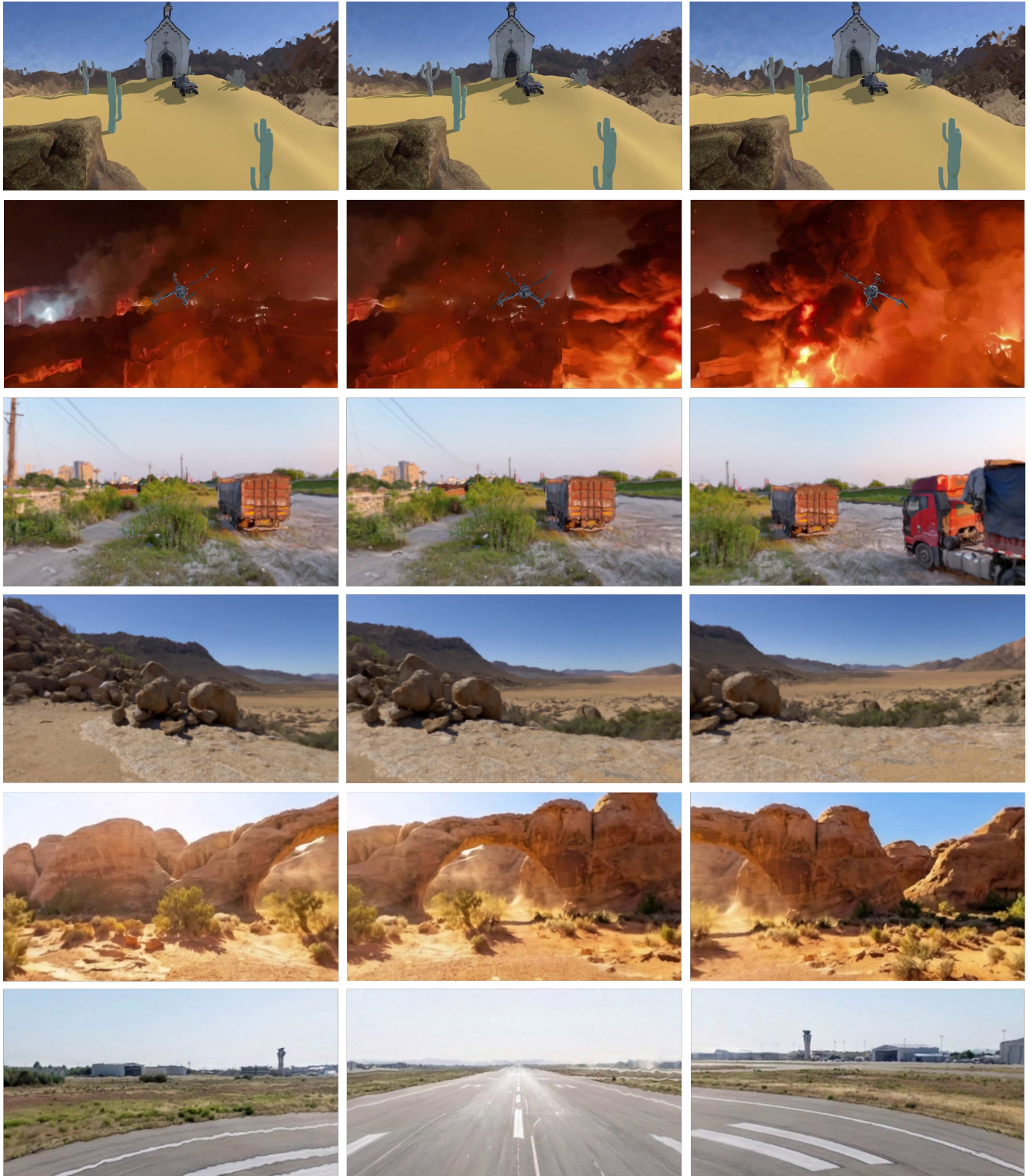


Figure 8. Simulation and rendering results of our heat-induced turbulence. Top two rows: rendering results from one camera along times. Bottom four rows: simulation results rendered from varying camera positions with different rotations, translations. More video results can be seen in the supplementary material.

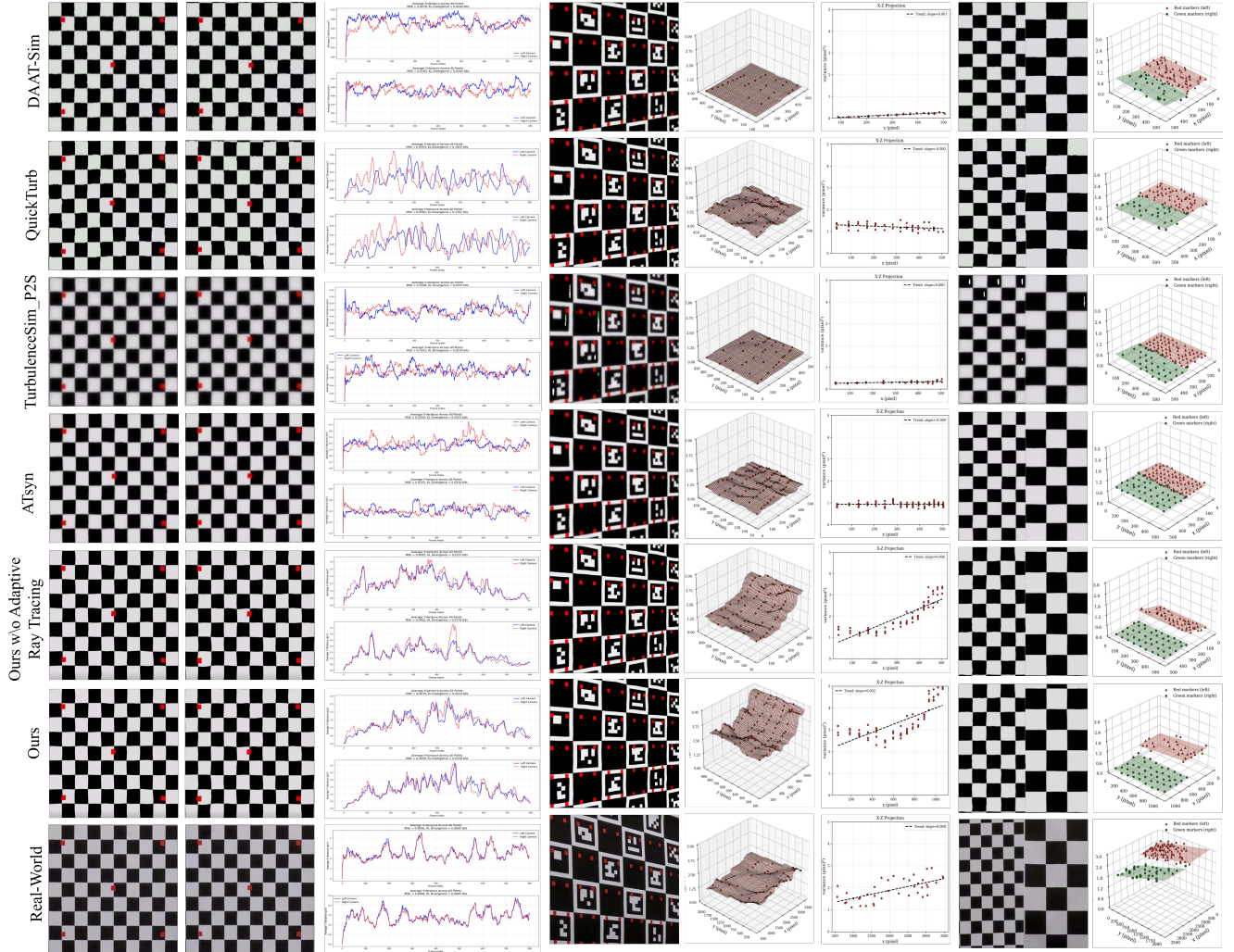


Figure 9. Qualitative analysis of our method compared with baselines and real-world results (zoom in for details). (Top) (a) **Multi-View Consistency**: two cameras with a small baseline capture turbulence-affected imagery; variance curves of tracked points along xy axes from our simulator overlap closely between cameras, matching real data. (b) **Continuous Depth**: with a tilted plane, variance projected onto the $x-z$ plane increases with distance, consistent with real-world trends. (c) **Discrete Depths**: with two parallel planes at different depths, simulator results show variance clustered on two separated planes, in agreement with real observations.

5. Conclusion

We have presented the first real-time simulator for heat-induced air turbulence that couples Smoothed Particle Hydrodynamics with curved ray tracing to achieve physically grounded 3D volume rendering. Our framework incorporates heat transport between source and particles as well as inter-particle exchange, enabling coherent multi-view turbulence effects at interactive frame rates. We will release our code publicly following peer review to facilitate future research and applications. Looking ahead, several promising directions remain. Our current design adopts approximate physics models (e.g., temperature-driven velocity updates, the Gladstone–Dale relation for refractive index, lin-

earized ideal gas law, and simplified heat-source modeling); extending these toward higher-fidelity formulations could yield a scientific-grade turbulence simulation. Beyond improving physical accuracy, our system opens opportunities for exploring challenging application domains, such as long-range (> 1 km) imaging and computer vision with high focal-length cameras. The multi-view consistency of our rendering also provides a platform for evaluating and advancing multi-view stereo algorithms under turbulence. Finally, adapting our approach to other thermally driven fluids (e.g., water) could broaden its impact to a wider range of graphics and scientific applications.

References

- [1] S Adami, X Hu, and N Adams. Simulating three-dimensional turbulence with sph. Technical report, Lehrstuhl für Aerodynamik, 2012. 2
- [2] Marco Ament, Christoph Bergmann, and Daniel Weiskopf. Refractive radiative transfer equation. *ACM Trans. Graph.*, 33(2), 2014. 3
- [3] Jan Bender, Dan Koschier, Tassilo Kugelstadt, and Marcel Weiler. Turbulent micropolar sph fluids with foam. *IEEE transactions on visualization and computer graphics*, 25(6): 2284–2295, 2018. 2
- [4] Marc Berger, Terry Trout, and Nancy Levit. Ray tracing mirages. *IEEE Computer Graphics and Applications*, 10(3): 36–41, 1990. 3
- [5] Manish Bhattarai, Aura Rose Jensen-Curtis, and Manel Martínez-Ramón. An embedded deep learning system for augmented reality in firefighting applications. In *2020 19th IEEE International Conference on Machine Learning and Applications (ICMLA)*, pages 1224–1230. IEEE, 2020. 2
- [6] Jeremy P Bos and Michael C Roggemann. Technique for simulating anisoplanatic image formation over long horizontal paths. *Optical Engineering*, 51(10):101704–101704, 2012. 3
- [7] Nicholas Chimitt and Stanley H Chan. Simulating anisoplanatic turbulence by sampling intermodal and spatially correlated zernike coefficients. *Optical Engineering*, 59(8): 083101–083101, 2020. 2
- [8] Nicholas Chimitt, Xingguang Zhang, Zhiyuan Mao, and Stanley H Chan. Real-time dense field phase-to-space simulation of imaging through atmospheric turbulence. *IEEE Transactions on Computational Imaging*, 8:1159–1169, 2022. 1, 2, 3
- [9] Simon Clavet, Philippe Beaudoin, and Pierre Poulin. Particle-based viscoelastic fluid simulation. In *Proceedings of the 2005 ACM SIGGRAPH/Eurographics Symposium on Computer Animation*, page 219–228, New York, NY, USA, 2005. Association for Computing Machinery. 2
- [10] Paul W Cleary and Joseph J Monaghan. Conduction modelling using smoothed particle hydrodynamics. *Journal of Computational Physics*, 148(1):227–264, 1999. 2
- [11] Paul W Cleary and Joseph J Monaghan. Conduction modelling using smoothed particle hydrodynamics. *Journal of Computational Physics*, 148(1):227–264, 1999. 4
- [12] Peter Davidson. *Turbulence: an introduction for scientists and engineers*. Oxford university press, 2015. 2
- [13] Richard P Feynman, Robert B Leighton, and Matthew Sands. *The Feynman lectures on physics, Vol. II: The new millennium edition: mainly electromagnetism and matter*. Basic books, 2015. 2
- [14] Basile Fraboni, Tsz Kin Chan, Thibault Vergne, and Jakub Jeziorski. Can you see the heat? a null-scattering approach for refractive volume rendering. In *ACM SIGGRAPH 2023 Talks*, New York, NY, USA, 2023. Association for Computing Machinery. 3
- [15] Robert A Gingold and Joseph J Monaghan. Smoothed particle hydrodynamics: theory and application to non-spherical stars. *Monthly notices of the royal astronomical society*, 181(3):375–389, 1977. 2
- [16] J. H. Gladstone and T. P. Dale. Researches on the refraction, dispersion, and sensitiveness of liquids. [abstract]. *Proceedings of the Royal Society of London*, 12:448–453, 1862. 5
- [17] Samuel J Grauer, Khadijeh Mohri, Tao Yu, Hecong Liu, and Weiwei Cai. Volumetric emission tomography for combustion processes. *Progress in energy and combustion science*, 94:101024, 2023. 2
- [18] Diego Gutierrez, Francisco J Seron, Adolfo Munoz, and Oscar Anson. Simulation of atmospheric phenomena. *Computers & Graphics*, 30(6):994–1010, 2006. 3
- [19] Russell C Hardie, Jonathan D Power, Daniel A LeMaster, Douglas R Droege, Szymon Gladysz, and Santasri Bose-Pillai. Simulation of anisoplanatic imaging through optical turbulence using numerical wave propagation with new validation analysis. *Optical Engineering*, 56(7):071502–071502, 2017. 3
- [20] Xiaowei He, Shusen Liu, Yuzhong Guo, Jian Shi, and Ying Qiao. A semi-implicit sph method for compressible and incompressible flows with improved convergence. *Computer Graphics Forum*, 44(2):e70043, 2025. 2, 5
- [21] Leila Jahanshaloo, Emad Pouryazdanpanah, and Nor Azwadi Che Sidik. A review on the application of the lattice boltzmann method for turbulent flow simulation. *Numerical Heat Transfer, Part A: Applications*, 64(11): 938–953, 2013. 2
- [22] JH Jeong, MS Jhon, JS Halow, and J Van Osdol. Smoothed particle hydrodynamics: Applications to heat conduction. *Computer Physics Communications*, 153(1):71–84, 2003. 2
- [23] Andrei Nikolaevich Kolmogorov. Dissipation of energy in the locally isotropic turbulence. *Proceedings of the Royal Society of London. Series A: Mathematical and Physical Sciences*, 434(1890):15–17, 1991. 2
- [24] Andrei Nikolaevich Kolmogorov. The local structure of turbulence in incompressible viscous fluid for very large reynolds numbers. *Proceedings of the Royal Society of London. Series A: Mathematical and Physical Sciences*, 434(1890):9–13, 1991. 2
- [25] Ares Lagae, Sylvain Lefebvre, Rob Cook, Tony DeRose, George Drettakis, David S Ebert, John P Lewis, Ken Perlin, and Matthias Zwicker. A survey of procedural noise functions. *Computer Graphics Forum*, 29(8):2579–2600, 2010. 3
- [26] Douglas Lanman and David Luebke. Near-eye light field displays. *ACM transactions on graphics (TOG)*, 32(6):1–10, 2013. 2
- [27] Sinuo Liu, Xiaokun Wang, Xiaojuan Ban, Yanrui Xu, Jing Zhou, Jiří Kosinka, and Alexandru C Telea. Turbulent details simulation for sph fluids via vorticity refinement. In *Computer Graphics Forum*, pages 54–67. Wiley Online Library, 2021. 2, 8
- [28] Shusen Liu, Xiaowei He, Yuzhong Guo, Yue Chang, and Wencheng Wang. A dual-particle approach for incompressible sph fluids. *ACM Trans. Graph.*, 43(3), 2024. 2
- [29] Leon B Lucy. A numerical approach to the testing of the fission hypothesis. *Astronomical Journal, vol. 82, Dec. 1977, p. 1013-1024.*, 82:1013–1024, 1977. 2

- [30] Miles Macklin and Matthias Müller. Position based fluids. *ACM Trans. Graph.*, 32(4), 2013. 2
- [31] Zhiyuan Mao, Nicholas Chimitt, and Stanley H Chan. Accelerating atmospheric turbulence simulation via learned phase-to-space transform. In *Proceedings of the IEEE/CVF International Conference on Computer Vision*, pages 14759–14768, 2021. 1, 3, 7
- [32] Joseph J Monaghan. Sph compressible turbulence. *Monthly Notices of the Royal Astronomical Society*, 335(3):843–852, 2002. 2
- [33] Joe J Monaghan. Smoothed particle hydrodynamics. *Reports on progress in physics*, 68(8):1703, 2005. 8
- [34] Joe J Monaghan. A turbulence model for smoothed particle hydrodynamics. *European Journal of Mechanics-B/Fluids*, 30(4):360–370, 2011. 2
- [35] Matthias Müller, David Charypar, and Markus Gross. Particle-based fluid simulation for interactive applications. In *Proceedings of the 2003 ACM SIGGRAPH/Eurographics Symposium on Computer Animation*, page 154–159, Goslar, DEU, 2003. Eurographics Association. 3
- [36] Matthias Müller, David Charypar, and Markus Gross. Particle-based fluid simulation for interactive applications. In *Proceedings of the 2003 ACM SIGGRAPH/Eurographics symposium on Computer animation*, pages 154–159. Cite-seer, 2003. 2
- [37] K.C. Ng, Y.L. Ng, T.W.H. Sheu, and A. Alexiadis. Assessment of smoothed particle hydrodynamics (sph) models for predicting wall heat transfer rate at complex boundary. *Engineering Analysis with Boundary Elements*, 111:195–205, 2020. 4
- [38] Matthias Oberhauser, Daniel Dreyer, Reinhard Brauningl, and Ioana Koglbauer. What’s real about virtual reality flight simulation? *Aviation Psychology and Applied Human Factors*, 2018. 2
- [39] Mark Olano, John C Hart, Wolfgang Heidrich, Bill Mark, and Ken Perlin. Real-time shading languages. *SIGGRAPH Course Notes*, 2002. 3
- [40] Adithya Pediredla, Yasin Karimi Chalmiani, Matteo Giuseppe Scopelliti, Maysamreza Chamanzar, Srinivasa Narasimhan, and Ioannis Gkioulekas. Path tracing estimators for refractive radiative transfer. *ACM Transactions on Graphics (TOG)*, 39(6):1–15, 2020. 3
- [41] Ken Perlin. An image synthesizer. *SIGGRAPH Comput. Graph.*, 19(3):287–296, 1985. 3
- [42] Tobias Pfaff, Nils Thuerey, Jonathan Cohen, Sarah Tariq, and Markus Gross. Scalable fluid simulation using anisotropic turbulence particles. In *ACM SIGGRAPH Asia 2010 Papers*, New York, NY, USA, 2010. Association for Computing Machinery. 1
- [43] Tobias Pfaff, Nils Thuerey, and Markus Gross. Lagrangian vortex sheets for animating fluids. *ACM Transactions on Graphics (TOG)*, 31(4):1–8, 2012. 8
- [44] Stephen B Pope. Turbulent flows. *Measurement Science and Technology*, 12(11):2020–2021, 2001. 8
- [45] Timo Probst and Matthias Teschner. Unified pressure, surface tension and friction for sph fluids. *ACM Trans. Graph.*, 44(1), 2024. 2
- [46] Markus Raffel. Background-oriented schlieren (bos) techniques. *Experiments in Fluids*, 56(3):60, 2015. 2
- [47] Ripon Kumar Saha, Dehao Qin, Nianyi Li, Jinwei Ye, and Suren Jayasuriya. Turb-seg-res: a segment-then-restore pipeline for dynamic videos with atmospheric turbulence. In *Proceedings of the IEEE/CVF Conference on Computer Vision and Pattern Recognition*, pages 25286–25296, 2024. 1, 2, 7
- [48] Ripon Kumar Saha, Yufan Zhang, Jinwei Ye, and Suren Jayasuriya. Daatsim: Depth-aware atmospheric turbulence simulation for fast image rendering. *Computer Graphics Forum*, 2025. 3, 7
- [49] Jason D Schmidt. *Numerical simulation of optical wave propagation with examples in MATLAB*. SPIE, 2010. 3
- [50] Francisco J Seron, Diego Gutierrez, Guillermo Gutiérrez, and Eva Cerezo. Implementation of a method of curved ray tracing for inhomogeneous atmospheres. *Computers & Graphics*, 29(1):95–108, 2005. 3
- [51] Christopher M Teixeira. Incorporating turbulence models into the lattice-boltzmann method. *International Journal of Modern Physics C*, 9(08):1159–1175, 1998. 2
- [52] Hendrik Tennekes and John Leask Lumley. *A First Course in Turbulence*. MIT Press, 1972. 2
- [53] Yuandong Tian, Srinivasa G Narasimhan, and Alan J Vannevel. Depth from optical turbulence. In *2012 IEEE Conference on Computer Vision and Pattern Recognition*, pages 246–253. IEEE, 2012. 7
- [54] Damien Violeau and Reza Issa. Numerical modelling of complex turbulent free-surface flows with the sph method: an overview. *International Journal for Numerical Methods in Fluids*, 53(2):277–304, 2007. 2
- [55] Xingyu Ye, Xiaokun Wang, Yanrui Xu, Jiří Kosinka, Alexandru C Telea, Lihua You, Jian Jun Zhang, and Jian Chang. Monte carlo vortical smoothed particle hydrodynamics for simulating turbulent flows. In *Computer Graphics Forum*, page e15024. Wiley Online Library, 2024. 2
- [56] Caiyun Yu, Yi Zong, Mingliang Duan, Lei Chen, and Jianxin Li. Adaptive ray tracing in freeform gradient-index media using an index directional derivative. *Optics Letters*, 49(19):5375–5378, 2024. 3
- [57] Xingguang Zhang, Nicholas Chimitt, Yiheng Chi, Zhiyuan Mao, and Stanley H Chan. Spatio-temporal turbulence mitigation: a translational perspective. In *Proceedings of the IEEE/CVF conference on computer vision and pattern recognition*, pages 2889–2899, 2024. 1, 7
- [58] ZL Zhang, K Walayat, C Huang, JZ Chang, and MB Liu. A finite particle method with particle shifting technique for modeling particulate flows with thermal convection. *International journal of heat and mass transfer*, 128:1245–1262, 2019. 2
- [59] Ye Zhao, Yiping Han, Zhe Fan, Feng Qiu, Yu-Chuan Kuo, Arie E Kaufman, and Klaus Mueller. Visual simulation of heat shimmering and mirage. *IEEE transactions on visualization and computer graphics*, 13(1):179–189, 2006. 2